Chinese Journal of Chemical Engineering 54 (2023) 127–135

Contents lists available at ScienceDirect

Chinese Journal of Chemical Engineering

journal homepage: www.elsevier.com/locate/CJChE

Full Length Article

Experimental study on the desulfurization and evaporation characteristics of $Ca(OH)_2$ droplets

Yilin Song, Yize Zhang, Hao Zhou *

State Key Laboratory of Clean Energy Utilization, Zhejiang University, Hangzhou 310027, China

ARTICLE INFO

Article history:
Received 8 December 2021
Received in revised form 23 March 2022
Accepted 29 March 2022
Available online 05 April 2022

Keywords:
Magnified digital in-line holography
Evaporation
Gas–liquid absorption reaction
$Ca(OH)_2$
Micro-droplet

ABSTRACT

The experiments were conducted to focus on the desulfurization and evaporation characteristics of lime slurry droplets at 298–383 K. We designed an evaporation-reaction chamber with quartz glass windows. The monodisperse slurry droplet stream was injected into the evaporation reaction chamber, and the inlet gas components (air, air + SO_2) were introduced into the chamber. We applied the magnified digital in-line holography to measure the droplet parameters and calculated the evaporation rate. The effects of temperature, droplet concentration, and SO_2 concentration on the evaporation rate of $Ca(OH)_2$ droplets were discussed. Moreover, the $Ca(OH)_2$ droplets under different experimental conditions were sampled, and the droplets were observed and analyzed using an off-line microscope. The evaporation rate of the Ca $(OH)_2$ droplet increased at first, and then decreased during the falling process, and remained constant at last. The average evaporation rate of the $Ca(OH)_2$ droplets increased significantly with the temperature increasing.

1. Introduction

Coal-fired power plants normally use flue gas desulfurization (FGD) methods. It mainly contains wet flue gas desulfurization (WFGD), dry sorbent injection (DSI), spray dryer absorption (SDA). WFGD is widely applied due to high SO_2 removal efficiency, reliability with less resource consumption [1]. In the WFGD process, limestone slurry is the absorbent; the flue gas enters the SO_2 absorption tower and contacts the absorbent within the tower in reverse. Subsequently, the SO_2 is captured in a liquid or water suspension of the active absorbent and reacts with the limestone slurry to form $CaSO_3$. Thereafter, $CaSO_3$ reacts with O_2 in the air to produce $CaSO_4{\cdot}2H_2O$, which is the byproduct of the desulfurization reaction. Finally, the flue gas is discharged into the atmosphere after defogging and removing SO_2. The major reactions involved in the WFGD method are as follows:

$$CaCO_3 + 2SO_2 + H_2O \rightarrow Ca(HSO_3)_2 + CO_2 \quad (1)$$

$$Ca(HSO_3)_2 + 1/2O_2 + H_2O \rightarrow CaSO_4 \cdot 2H_2O + SO_2 \quad (2)$$

$$Ca^{2+} + SO_4^{2-} + 2H_2O \rightarrow CaSO_4 \cdot 2H_2O \quad (3)$$

The DSI method involves uniformly spraying a high-efficiency absorbent into the flue duct; $NaHCO_3$ or $Ca(OH)_2$ is often used as the absorbent. First, the absorbent is thermally activated in the flue duct such that its specific surface area increases rapidly. Second, the absorbent contacts the acidic flue gas sufficiently and reacts with the acidic substances. Third, the dried powder-containing flue gas after chemical reaction goes to the dust collector for further desulfurization and dust removal. Lastly, the eliminated flue gas goes to the atmosphere with an induced draft fan. For example, when $NaHCO_3$ is used as the absorbent, the major reactions involved in the DSI method are as follows:

$$2NaHCO_3 + SO_2 + 1/2O_2 \rightarrow Na_2SO_4 + 2CO_2 + H_2O \quad (4)$$

$$2NaHCO_3 + SO_3 \rightarrow Na_2SO_4 + 2CO_2 + H_2O \quad (5)$$

$$NaHCO_3 + HCl \rightarrow NaCl + CO_2 + H_2O \quad (6)$$

$$NaHCO_3 + HF \rightarrow NaF + CO_2 + H_2O \quad (7)$$

The SDA method is often regarded as the trend of future development and offers benefits such as low initial investment, low operating cost, no corrosion, no heating of the flue gas after desulfurization, and high desulfurization efficiency; thus, it has become the most widely used desulfurization method, with the exception of WFGD [2–4]. In the desulfurization process of the SDA method, the lime slurry is atomized into microdroplets with particle sizes of

* Corresponding author. Fax: +86 571 87951616.
E-mail address: zhouhao@zju.edu.cn (H. Zhou).

https://doi.org/10.1016/j.cjche.2022.03.020
1004-9541/

20–50 μm under the action of the centrifugal force of a rapidly rotating atomizer; many $Ca(OH)_2$ particles are distributed in the lime slurry droplets. The SO_2 in the flue gas dissolves in the droplets and reacts with $Ca(OH)_2$ to produce $CaSO_3$. Simultaneously, the droplets evaporate under the action of the hot flue gas. Lastly, the $CaSO_3$ reacts with O_2 in the air to produce $CaSO_4{\cdot}2H_2O$. The major reactions involved in the SDA method are as follows:

$$Ca(OH)_2 + SO_2 + H_2O \rightarrow CaSO_3 \cdot 2H_2O \quad (8)$$

$$CaSO_3 \cdot 2H_2O + 1/2O_2 \rightarrow CaSO_4 \cdot 2H_2O \quad (9)$$

Several studies have been conducted to assess the desulfurization and evaporation characteristics of lime slurry droplets in the SDA method. On the one hand, models have been developed in some studies to investigate the transformation of the heat mass of the flue gas/lime slurry droplets [4–7]. On the other hand, experimental investigations have been reported on the gas–liquid absorption reactions of lime slurry droplets [8–13]. The effects of inlet gas temperature, the flow rate of the slurry, the mean diameter of the spray droplets, and the inlet concentration of SO_2 on the desulfurization efficiency have been discussed [8–11]. Liu *et al.* [12] and Dagaonkar *et al.* [13] reported the effects of adding fly ash or solid particles to the lime droplets on the gas–liquid absorption reaction rates. Previously, the experiments were mainly conducted with fixed bed reactors or pilot-scale spray drying absorbers; in these approaches, it is difficult to focus on the desulfurization characteristics of the individual slurry droplets to show the mechanism of the desulfurization reaction process.

The free-falling method [14] involves studying the evaporation of the droplets; in this method, monodisperse droplets are generated and allowed to fall freely in the evaporation chamber. The evaporation process of the droplets is similar to that in the SDA method. Furthermore, the free-falling is fitted for studying the evaporation of droplets under small diameters (~50 μm), which are similar to the diameters of the lime slurry droplets after atomization. Consequently, the free-falling method is used to investigate the evaporation and gas–liquid absorption reaction processes of lime slurry droplets of diameters ~50 μm.

From a measurement perspective, the study of droplet evaporation essentially relies on the three-dimensional positions, particle sizes, and velocities. A more widely used technique is the phase doppler anemometry (PDA) [15], whose advantages include high accuracy, high spatial resolution, wide measurement range, and fast dynamic response. However, the PDA only provides a single-point measurement, *i.e.*, only one location in space can be measured at any given moment. To track the particle size over the entire droplet trajectory, an automatically controlled scanning measurement is required, which is a lengthy procedure. The digital in-line holography (DIH) is an efficient technique to measure the droplet parameters over the entire measurement area [16–18]; it is a secondary imaging technique that uses the interference principle of light to record and reproduce the phase information of the object light accurately. The droplet size and spatial distribution can be derived by analyzing the captured hologram. Based on an extension of the DIH, a technique with high magnification of the lens mechanism is introduced, which is known as magnified digital in-line holography (MDIH) [17]. The MDIH not only improves the accuracy of measurement of small-sized droplet particles but also increases the depth of field and allows a longer distance between the object and measurement element.

In this study, we conduct experiments to focus on the desulfurization and evaporation characteristics of lime slurry droplets from 298 to 383 K. We designed an evaporation reaction chamber with quartz glass windows; the monodisperse slurry droplet stream was injected into the evaporation reaction chamber, and the inlet gas components (air, air + SO_2) were introduced into the reactor. We applied the MDIH method to measure the droplet parameters and calculated the evaporation rate. The effects of temperature, droplet concentration, and SO_2 concentration on the $Ca(OH)_2$ droplets evaporation rates were discussed. Moreover, the $Ca(OH)_2$ droplets were sampled under different experimental conditions, and the droplets were observed and analyzed using an offline microscope.

2. Experimental

2.1. Materials

The saturated $Ca(OH)_2$ solution was prepared at 298 K, with a solubility of 1.6 $g{\cdot}L^{-1}$ [19]. To study the effect of $Ca(OH)_2$ concentration on the evaporation process, $Ca(OH)_2$ solutions with mass fractions of 0.16% and 0.08% were prepared, corresponding to saturated and unsaturated $Ca(OH)_2$, respectively. $Ca(OH)_2$ (analytical reagent, purity ≥95.0%; Sinopharm Chemical Reagent Co., Ltd., China) was weighed using an electronic balance and dissolved in deionized water (DI) to prepare solutions. Electronic balance: Mettler Toledo AL204 (Switzerland), the accuracy of 0.1 mg. The $Ca(OH)_2$ was slightly dissolved in DI water. To prevent contamination or clogging of the nozzle by the incompletely dissolved $Ca(OH)_2$, the solution was extracted 24 h after preparation and filtered by a 0.22 μm syringe filter.

2.2. Experimental apparatus and conditions

2.2.1. Experimental equipment

It is a schematic experimental system in Fig. 1. It mainly contains one heating furnace, one droplet generation system, one gas supply system, one gas distribution system, and an MDIH measurement system. The reaction chamber with the size of 200 mm × 200 mm × 1000 mm has two of 4 mm thick, 100 mm wide, and 800 mm high S1 square quartz windows. A sampling port is set at the bottom of the reaction chamber, and droplets under different experimental conditions are sampled using slides and analyzed using an off-line microscope. The chamber is electrically heated using a PID controller with an accuracy of ±1 K. Three thermocouples are mounted at 100 mm (marked as A), 400 mm (marked as B), and 700 mm (marked as C) from the top of the evaporation chamber. The reaction temperature was controlled precisely. The heating power of the evaporation chamber is adjusted by the PID controller, and the temperature of the thermocouple B is the setting temperature. Two ALICAT (USA) mass flow controllers (MFC) with an accuracy of ±0.5% are used to control the gas flow rates. The airflow is preheated in an industrial heater before entering the chamber, and then passes through the rectifier structure and heating furnace. Lastly, the airflow is discharged from the furnace through the induced draft fan. A valve is set in the front of the induced draft fan to control the gas velocity, and the gas flow rate in the chamber is set to 2.7 $m{\cdot}s^{-1}$.

The monodisperse slurry droplets are generated using a piezoelectric injection device manufactured by MicroFab Technologies (MicroFab Inc., Plano, Texas, USA). According to the work of Chareyron [20], the monodisperse droplets are stable. Its diameters are approximately the same as the nozzle orifice. The standard deviation of the droplet diameters from the nozzle orifice diameter is 0.5 μm [20]. The nozzle is protected from high-temperature damage by a cooling aluminum with internal cooling water. Electrical pulse signals of frequency 1000 Hz were applied to the nozzle using a Jet Drive V controller (MicroFab). To produce stable and reproducible droplets, the optimal waveform for the 0.16% (mass) $Ca(OH)_2$ solution is shown in Fig. 2. A pressure controller (MicroFab) was used to adjust the pressure of the nozzle. The solid

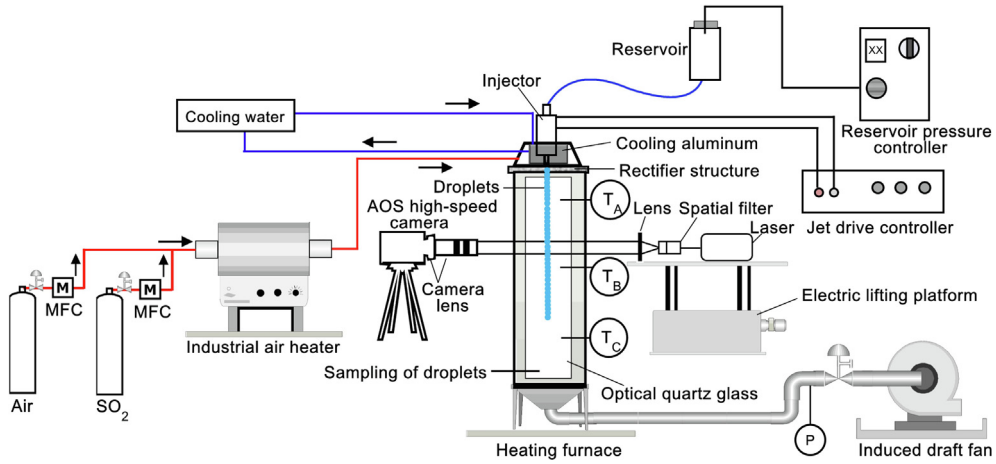

Fig. 1. The schematic diagram of the experimental system.

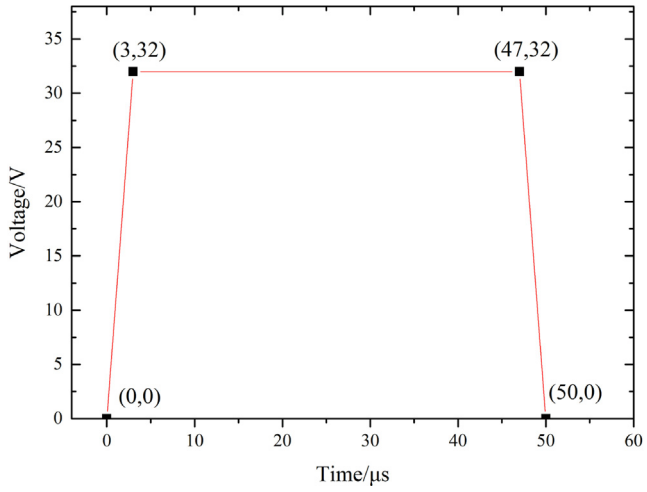

Fig. 2. The waveform parameter for $Ca(OH)_2$ droplets.

particles in the $Ca(OH)_2$ solution were filtered using a disposable (pore size is 0.22 μm) syringe filter. Images of injecting the 0.16% (mass) $Ca(OH)_2$ droplets, which were captured using a charge-coupled device (CCD, MicroFab), are shown in Fig. 3. It is observed that the shape of the droplets during the fall is approximately spherical. The solution is then stored in a reservoir.

2.2.2. MDIH measurements

The measurement of the MDIH technique includes the recording process and reconstruction process of the hologram. The recording progress can be expressed as:

$$H(x,\ y) = R(x,\ y) + O(x,\ y) \tag{10}$$

where $H(x, y)$ is the hologram wavefield; $R(x, y)$ and $O(x, y)$ are reference beam wavefield and object beam wavefield, respectively.

Supposing the light intensity on the particle plane is $P(x, y)$, the light intensity on the recording plane $I_z(x, y)$ can be expressed as:

$$I_z(x,\ y) = 1 - \frac{2}{\lambda z} P(x,\ y) \otimes \sin[\frac{\pi}{\lambda z}(x^2 + y^2)] \tag{11}$$

where z is the distance between the particle plane and the recording plane; λ is the laser wavelength; $\otimes$ is the convolution operation.

The arrangement of the MDIH optical system comprising a 532 nm laser beam (Laserwave Optoelectronics Technology Co., Ltd., Beijing, China), a spatial filter, a lens, a combined camera lens, and a high-speed CCD camera (AOS S-PRI plus), as shown in Fig. 1. The combination lens comprises a micro-zoom lens (LMZ45T3, KOWA, Japan) and a 5 × magnification lens to provide magnification. The power of the laser was set to 1.0 W. The resolution of the high-speed CCD camera is 800 × 600 pixels (14 μm·pixel^{-1}), the frequency of the camera is 1250 frames per second, and the camera exposure time is 10 μs. To perform the measurements of droplet parameters along the centerline of the chamber, a high-precision motorized vertical stage (PSA400-11-Z, Zolix Instruments Co., Ltd., China) is used to adjust the height of the laser. A tripod is used for the camera in order to match the parallel beam. Finally, the captured holograms are post-processed to obtain the relevant droplet parameters. More detailed information about hologram post-processing could be found in our previous work [21].

The magnification of the combined lens was calibrated with a micrometer, which has a calibration target with a graduation every 100 μm. During the magnification calibration process, the micrometer was placed on the optical rail 100 mm away from the lens. By

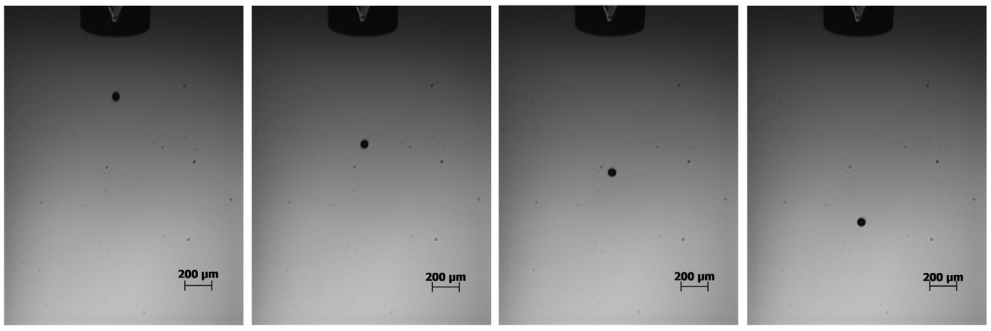

Fig. 3. Images of the droplet jet.

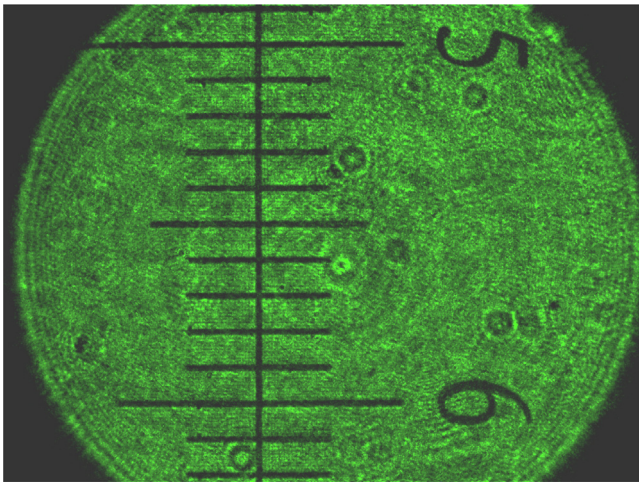

Fig. 4. The micrometer calibration ruler.

adjusting the camera lens, the magnification factor and focus can be changed. When the micrometer image is clearly visible, the camera lens is fixed, and the position of the micrometer is the focus. Fig. 4 shows an image of the calibration ruler after magnification. The magnification was calculated according to the procedure noted in our previous work [14]. The average magnification value was 6.30 through 10 times of calibrations. The camera field of view was 11.2 mm × 8.4 mm, and later it was changed to 1.78 mm × 1.33 mm. The magnification was proximate 2.22 μm·pixel^{-1}.

2.2.3. Experimental procedures

First, the height of the laser was adjusted to the height of top of the quartz glass for the first measurement. Then, the height was lowered by 50 mm for the second measurement using the high-precision motorized vertical stage. Simultaneously, the camera tripod was manually adjusted to align the camera height with that of the laser beam. By analogy, ten different positions were measured, 450 mm long area was measured. Minimum 15 holograms were selected and reconstructed at any measurement points. Taken into consideration that the field of view of the camera was small in the MDIH optical system, and the droplet size could not change significantly at each location, the average particle size of all the holograms, therefore, represented the average diameter of the imaged area. Each point was measured a minimum of 3 times under different conditions. Moreover, $Ca(OH)_2$ droplets under different experimental conditions were sampled on the glass at the bottom of the furnace and analyzed using an off-line microscope. The droplets were collected on a glass slide, and the temperature of the substrate was 298 K. The images were recorded approximately 2 min after the droplet impacts. The effects of the operating conditions, such as heating temperature, slurry concentration, and SO_2 inlet concentration, were investigated. The experimental conditions are summarized in Table 1.

3. Results and Discussion

3.1. Hologram reconstruction

In this work, the hologram is a rigorous solution simulated by the Lorenz–Mie theory (LMT) [21], which is used for spherical particles illuminated by the Gaussian beam. There is no accurate solution to the scattering caused by irregular particles. However, evaporating falling droplets undergo shape oscillations [22–26]. The shape oscillations have an effect on the evaporation process. In this work, the morphology of droplets is assumed to be spherical without deformation. On the one hand, droplets were almost spherical by observing particle morphology, as shown in Fig. 3. After binarizing the images, the roundness of the droplets was measured using ImageJ software. According to the measurement results, the roundnesses of the droplets were 0.822, 0.988, 0.931, and 0.941, respectively. We think that the shape oscillation of the droplet was not obvious. On the other hand, unlike water droplets, there were particles accumulating on the surface of $Ca(OH)_2$ droplets during evaporation. Particles on the droplet surface reduce the effect of shape oscillations. In addition, the dynamics of evaporating falling droplets has been studied [22–26]. Balla *et al.* [22] and Agrawal *et al.* [23] investigated the dynamics of non-spherical droplets falling in air. They found that the shape oscillation of droplets with a small degree of nonsphericity was small during the falling process. The droplets with a large degree of nonsphericity underwent prolate-oblate-prolate deformations as time progressed. Tripathi *et al.* [24] used numerical simulation to study the dynamics of evaporating falling droplets. The results indicated that the droplets deformed slightly to an oblate shape during the falling process, as shown in Fig. 5. Balla *et al.* [25] numerically studied the dynamics of a hollow water droplet. Agrawal *et al.* [26] investigated the shape oscillation of droplets due to the propulsive force. The shape of the droplet is either oblate or prolate. Thus, we think that it is suitable for assuming that the droplets are spherical without deformation. Thus, we think that it is suitable for assuming that the droplets are spherical without deformation.

The holographic reconstructed image sequence for a $Ca(OH)_2$ droplet is shown in Fig. 6. First, a hologram was obtained as a background image without the droplet. Then, the hologram was corrected from the background image to obtain a background-corrected hologram without scratches, dust, and other disturbances. Finally, the background-corrected hologram was reconstructed using wavelet transform [27,28].

In the wavelet transform, the wavelet function can be expressed as:

$$\psi_k(x,y) = \frac{1}{k^2}\sin\left(\frac{x^2+y^2}{k^2}\right) \tag{12}$$

where k is the scale parameter, which can be expressed as:

$$k = \sqrt{\frac{\lambda z}{\pi}} \tag{13}$$

Table 1
Experimental conditions

Influencing factors	Temperature/K	Mass concentration of $Ca(OH)_2$/%	Concentration of SO_2/mg·m^{-3}
Mass concentration of $Ca(OH)_2$	298	0.08, 0.16	0
Temperature (without SO_2)	298, 323, 343, 363, 383	0.16	0
Concentration of SO_2	298	0.16	0, 286, 571
Temperature (with SO_2)	298, 343, 383	0.16	286

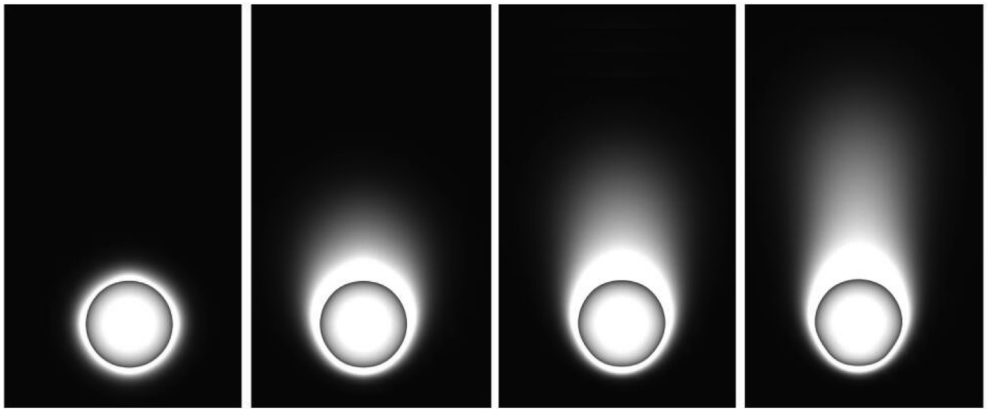

Fig. 5. The time evolution of the shape of the drop along with the vapour volume fraction [24].

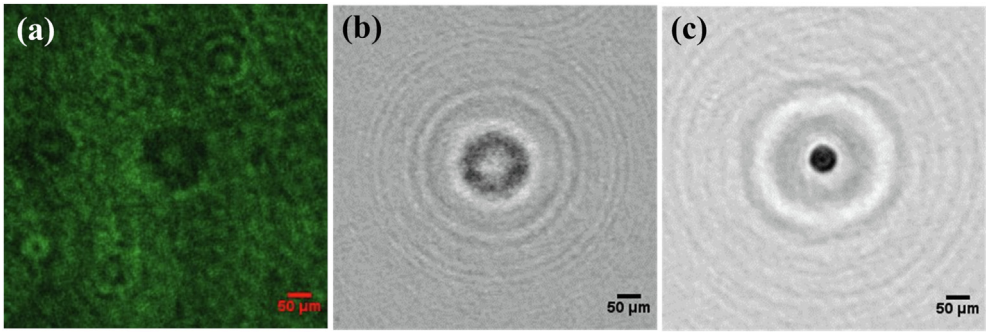

Fig. 6. Hologram reconstruction sequence images of a $Ca(OH)_2$ droplet: (a) raw hologram; (b) background corrected hologram; (c) reconstructed hologram.

According to the literature [28], the best recording distances were calculated as z_{crt} = 7.41 mm and 1.6 z_{crt} = 11.86 mm. A total of 440 reconstructed droplet holograms were sampled, and their probability distribution histogram and fitted Gaussian curve for the depths of the holograms are shown in Fig. 7. The reconstructed range of the droplets along the depth direction is 0–28 mm, and approximately 81% of the droplets are in the range of 4–16 mm, indicating that the holographic measurements are accurate with low uncertainties.

3.2. Droplet velocity of DI water and $Ca(OH)_2$

The velocities of DI water [14] and 0.16% (mass) $Ca(OH)_2$ droplets at 298 K are shown in Fig. 8. The $Ca(OH)_2$ droplet fall velocity first decreases and then remains constant. The decrease in droplet velocity is influenced mainly by the drag force in the air. The final drag force is balanced with the gravity of the droplet, which maintains the droplet in a steady-state evaporation process. The difference in the initial particle sizes of the droplets results in a slightly greater velocity of the $Ca(OH)_2$ droplets than that of DI water.

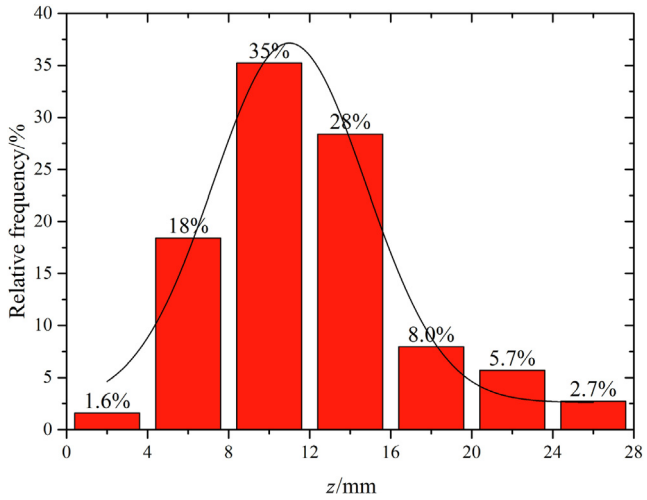

Fig. 7. Probability distribution histograms and fitted gaussian curve of the recording distance of holograms.

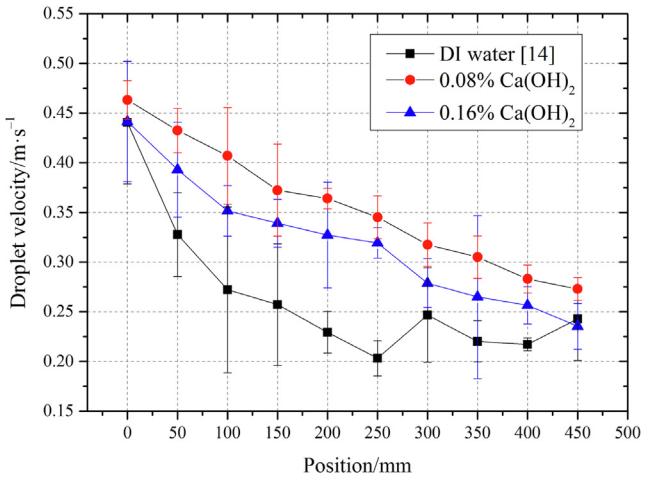

Fig. 8. The mean and standard deviations of the droplet velocity of deionized water [14] and $Ca(OH)_2$ in different mass concentrations at 298 K.

3.3. Effect of $Ca(OH)_2$ mass concentration on the evaporation process

The diameters of DI water [14], 0.08% (mass) $Ca(OH)_2$, and 0.16% (mass) $Ca(OH)_2$ droplets at different concentrations are shown in Fig. 9, and the calculated evaporation rates of the droplets at different positions are shown in Fig. 10. The "d^2" law has indicated that the square of the droplet diameter decreased linearly with time [16,17]. The linear fit was performed on the squared-diameters-over-time curves for each position to compare the evaporation rate. The slope of the linear fit represented the average evaporation rate for each location. A series of measurements for each location were taken under the same conditions. The droplet evaporation rate at each position was calculated, and the results showed that the evaporation rate of the $Ca(OH)_2$ droplets first increased, then decreased, and finally remained constant. The evaporation process of the $Ca(OH)_2$ droplets could be roughly divided into three stages as below.

(1) First stage: The injected droplets caused forced convection against the air and had the maximum evaporation rate. The droplet had a brief non-steady-state at the beginning of evaporation, and the evaporation rate of the droplets first decreased and then increased. The reason was that there was the largest temperature gradient and concentration gradient between the droplet surface and the surrounding environment at the beginning of the evaporation. The temperature gradient and concentration gradient decreased rapidly in the non-steady-state, resulting in a decrease in the evaporation rate. As the evaporation process progressed, the temperature gradient and concentration gradient were in a relatively balanced process, and the evaporation rate gradually increased. Unfortunately, due to the rapid decrease of the evaporation rate at the stage of the non-steady-state, the rapid decrease of the evaporation rate was not measured. After that, the droplets were in a relatively stable evaporation stage.

(2) Second stage: As the evaporation proceeded, a large amount of vapor accumulated around the droplets, and the concentration gradient around the droplets decreased rapidly. The vapor diffusion rate was less than the evaporation rate of the droplets. $Ca(OH)_2$ particles inside the droplets began to precipitate, and the particulate matter precipitated on the surface hinders water evaporation, thereby decreasing the evaporation rate.

(3) Third stage: The temperature gradient and concentration gradient between the droplet and the surrounding environment reached a relative equilibrium state. The vapor diffusion rate near the droplets was equal to the droplet evaporation rate; hence, the evaporation rate remained almost constant.

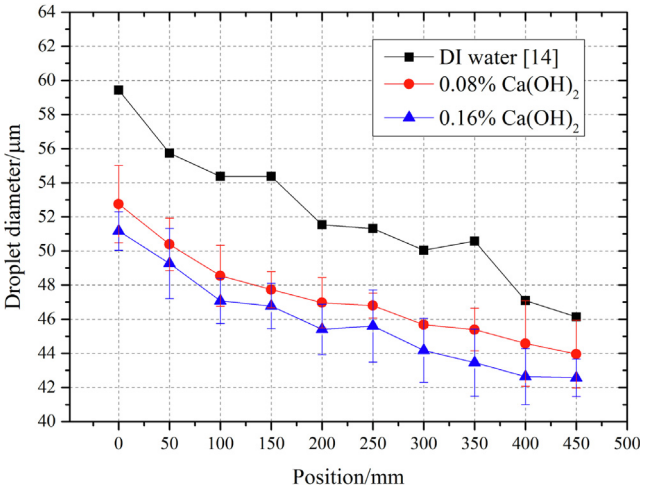

Fig. 9. The mean and standard deviations of the droplet diameters of deionized water [14] and $Ca(OH)_2$ in different mass concentrations at 298 K.

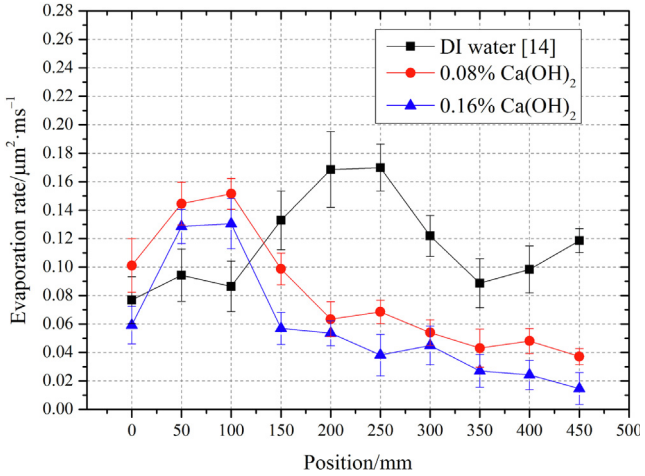

Fig. 10. The evaporation rates of deionized water [14] and $Ca(OH)_2$ in different mass concentrations at 298 K.

The evaporation rate of DI water droplets first increased and then decreased. The evaporation process of DI water droplets also had three stages, which was consistent with the trend of the evaporation rate of $Ca(OH)_2$ droplets. However, in the second stage, the falling distance where the evaporation rate of DI water droplets decreased was farther, and the residence time was longer in the furnace. It indicated that the evaporation resistance of DI water droplets was less than that of $Ca(OH)_2$ droplets in the second stage. As the evaporation proceeded, a large amount of steam accumulated around the DI water droplets, and the concentration gradient around the droplets decreased rapidly, thereby reducing the evaporation rate. In contrast, the influencing factors for the evaporation resistance of $Ca(OH)_2$ droplets were not only the vapor concentration but also the particulate matter precipitated on the $Ca(OH)_2$ surface.

The highest evaporation rates noted were (0.1699 ± 0.0165) $\mu m^2 \cdot ms^{-1}$ for DI water [14], (0.1515 ± 0.0108) $\mu m^2 \cdot ms^{-1}$ for 0.08% (mass) $Ca(OH)_2$ droplets, and (0.1305 ± 0.0176) $\mu m^2 \cdot ms^{-1}$ for 0.16% (mass) $Ca(OH)_2$ droplets. The average evaporation rates were (0.1199 ± 0.0322) $\mu m^2 \cdot ms^{-1}$ for the DI water [14], (0.0810 ± 0.04135) $\mu m^2 \cdot ms^{-1}$ for the 0.08% (mass) $Ca(OH)_2$ droplets, and (0.0577 ± 0.04056) $\mu m^2 \cdot ms^{-1}$ for the 0.16% (mass) $Ca(OH)_2$ droplets. These results indicated that the evaporation rates of the $Ca(OH)_2$ droplets were lower compared to that of DI water, and the average evaporation rates of 0.08% (mass) and 0.16% (mass) $Ca(OH)_2$ droplets were about 0.676 and 0.481 times that of DI water, respectively.

3.4. Discussion of the temperature impacts on the $Ca(OH)_2$ evaporation process

The diameters of DI water [14], 0.08% (mass) $Ca(OH)_2$, and 0.16% (mass) $Ca(OH)_2$ droplets are shown in Fig. 11, and the calculated droplet evaporation rates are shown in Fig. 12. The average evaporation rates of the $Ca(OH)_2$ droplets increased significantly with an increase in temperature, and the average evaporation rate of DI

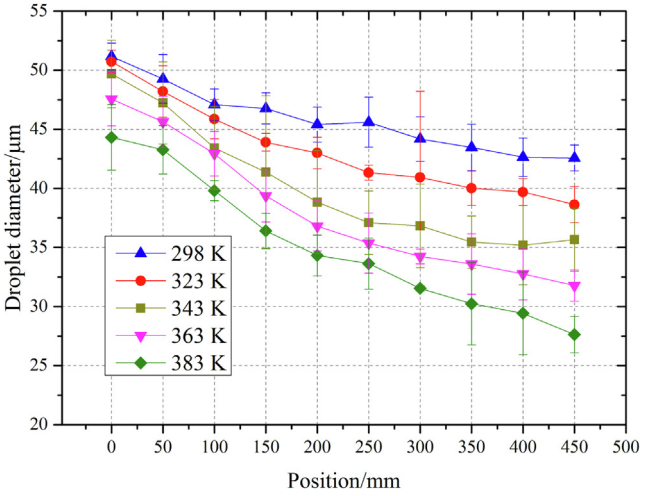

Fig. 11. The mean and standard deviations of the droplet diameters of 0.16% (mass) $Ca(OH)_2$ at different temperatures.

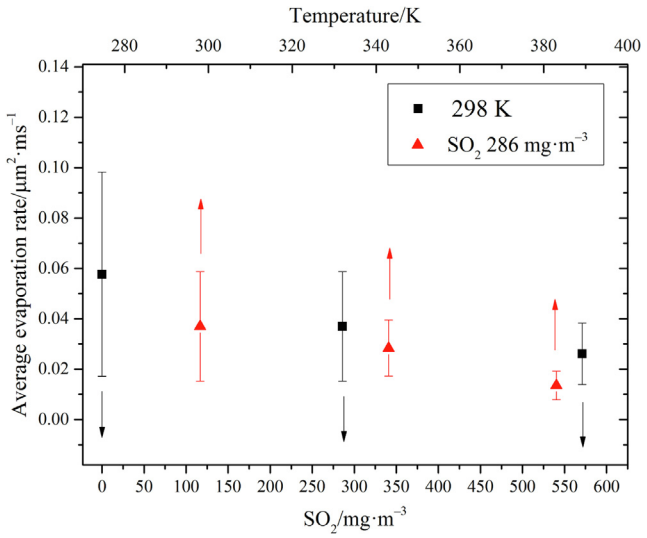

Fig. 13. The average evaporation rates of $Ca(OH)_2$ droplets at different SO_2 concentrations and temperatures.

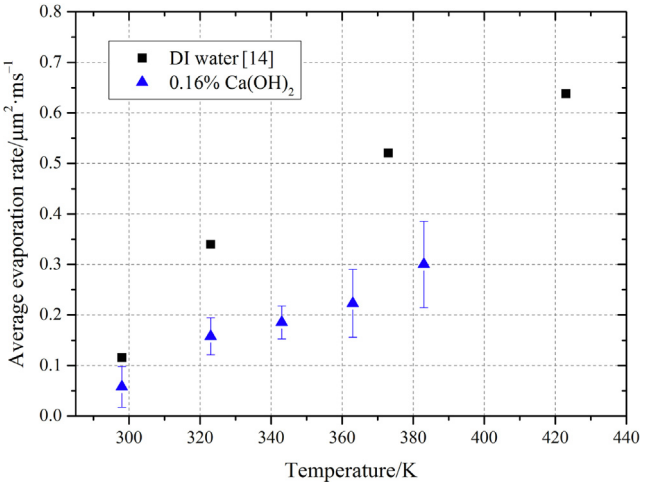

Fig. 12. The average evaporation rates of deionized water [14] and 0.16% (mass) $Ca(OH)_2$ at different furnace temperatures.

water was significantly greater than the $Ca(OH)_2$ droplets. The average evaporation rate of the $Ca(OH)_2$ droplets was highest at 383 K, which was (0.30018 ± 0.08561) $\mu m^2 \cdot ms^{-1}$. The average evaporation rate of the DI water at 373 K was 0.5204 $\mu m^2 \cdot ms^{-1}$. The average evaporation rate of the $Ca(OH)_2$ droplets is about 0.5 times that of DI water, and the evaporation rate of $Ca(OH)_2$ droplets at 383 K is about five times that at 298 K.

3.5. Discussion of the SO_2 concentration impacts on the evaporation and reaction process of $Ca(OH)_2$ droplets

The effects of different SO_2 concentrations on evaporation of the slurry droplets and desulfurization reaction were investigated at the SO_2 concentrations of 286 and 571 $mg \cdot m^{-3}$ at 298 K. In addition, the temperature of the reactor was set at 298, 343, and 383 K to investigate the effect of temperature on the evaporation and reaction process of $Ca(OH)_2$ droplets under the SO_2 concentration of 286 $mg \cdot m^{-3}$. The average evaporation rates of the $Ca(OH)_2$ droplets at different SO_2 concentrations and temperatures are shown in Fig. 13. In the presence of SO_2, the average $Ca(OH)_2$ droplets evaporation rate was lower than the rate when there was no introduction of SO_2. The average droplet evaporation rate at 298 K with 286 $mg \cdot m^{-3}$ SO_2 was (0.03699 ± 0.02175) $\mu m^2 \cdot ms^{-1}$. At 383 K, the average droplet evaporation rate at 286 $mg \cdot m^{-3}$ SO_2 was (0.01353 ± 0.0568) $\mu m^2 \cdot ms^{-1}$. As the temperature increased from 298 to 383 K, the average droplet evaporation rate decreased by 63.42%. For a given temperature, the evaporation rate decreased as the SO_2 concentration increased. The average droplet evaporation rates at 298 K for SO_2 concentrations of 0 and 571 $mg \cdot m^{-3}$ were (0.05774 ± 0.04056) and (0.02610 ± 0.01216) $\mu m^2 \cdot ms^{-1}$, respectively. Thus, when the SO_2 concentration increased from 0 to 571 $mg \cdot m^{-3}$, the average droplet evaporation rate decreased by 54.80%. This decrease might be attributed to the formation of $CaSO_3 \cdot 2H_2O$ crystals owing to the reactions on the droplet surfaces; these reactions increased the diffusion resistance of water vapor through the product layer and caused difficulties for SO_2 to diffuse to the interior of the slurry for continued reactions with the absorber. Therefore, when SO_2 gas was introduced, the evaporation rate of the slurry droplets was significantly reduced. When the concentration of SO_2 gas increasesd, the product layer on the surface of the slurry droplet was thicker, thereby reducing the evaporation rate of the slurry further.

As the temperature increased, the average evaporation rate increased in the absence of SO_2 (Section 3.4). On the contrary, as the temperature increased, the average evaporation rate decreased in the presence of SO_2. It is due to the fact that the increase in temperature accelerates the water evaporation in the absence of SO_2, resulting in an increase in the evaporation rate. However, the increase in temperature accelerates the gas–liquid reaction rate in the presence of SO_2, which causes the crystals on the surface of the slurry droplet to form more quickly and accumulate more, thus hindering the water evaporation. Therefore, the increase in temperature in the presence of SO_2 accelerates not only the evaporation of the water from the slurry droplet but also the gas–liquid absorption reaction rate, thereby reducing the evaporation rate of the slurry droplet.

3.6. $Ca(OH)_2$ droplet sampling and analysis

The $Ca(OH)_2$ droplets at the bottom of the furnace chamber were sampled under four operating conditions, as shown in

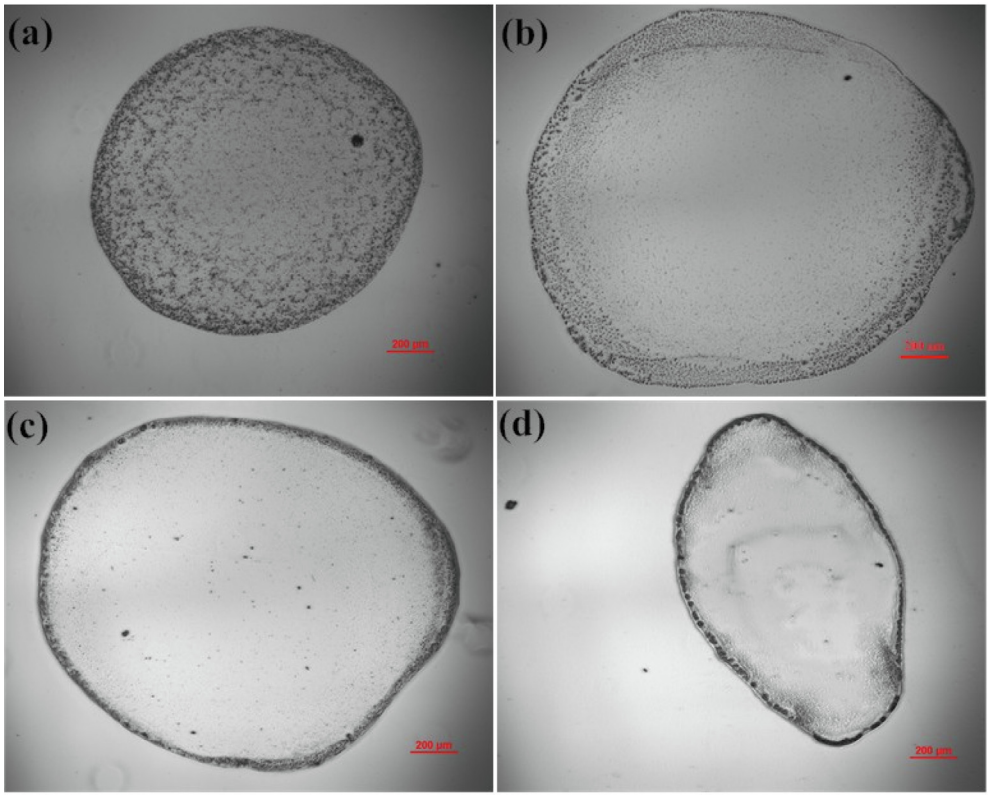

Fig. 14. Microscopic images of $Ca(OH)_2$ droplets: (a) 298 K, 0 mg·m^{-3} SO_2; (b) 298 K, 286 mg·m^{-3} SO_2; (c) 298 K, 571 mg·m^{-3} SO_2; (d) 383 K, 286 mg·m^{-3} SO_2.

Fig. 14. These four working conditions were 0, 286, and 571 mg·m^{-3} of SO_2 at 298 K as well as 286 mg·m^{-3} of SO_2 at 383 K. Through observations, it was found that there were many crystals in the $Ca(OH)_2$ droplets in the air, which were analyzed as $Ca(OH)_2$ particles. As the evaporation proceeded, $Ca(OH)_2$ accumulated on the droplet surface. Then, $Ca(OH)_2$ was precipitated on the droplet surface in the form of particles or even solid shells. Particles were opaque and non-evaporating material. Particles and solid shells on the droplet surface [29,30] led to an increase in the evaporation resistance of the remaining moisture inside the droplet. Consequently, particles on the droplet surface led to a decrease in the evaporation rate of the droplet.

However, there were fewer internal crystals in the $Ca(OH)_2$ droplets with SO_2, and the crystals on the surfaces of these droplets increased significantly, indicating that the SO_2 and $Ca(OH)_2$ droplets underwent gas–liquid absorption reactions on the surface to form $CaSO_3{\cdot}2H_2O$ crystals. When the concentration of SO_2 increased, the number of particles on the surfaces of the slurry droplets increased, and the product layer became thicker. When the temperature increased, the products on the $Ca(OH)_2$ droplets surface increased, the crystal particles were larger, and the product layer became thicker. The product layer not only hindered the evaporation of water inside the $Ca(OH)_2$ droplet but also reduced the contact area between the droplet surface and the surrounding environment. Therefore, particles on the droplet surface with SO_2 led to a more significant reduction in the evaporation rate. Some researchers studied the contact line of droplets and the crystallization process on a transparent substrate [31–33]. Tavakoli *et al.* [31] studied the forced spreading of alkanes on glass. In their work, it was assumed that solidification starts from the contact line. The droplet would stop spreading once a critical volume of liquid at the contact line is solidified. In Fig. 14(d), when the temperature increased, the products on the $Ca(OH)_2$ droplets surface increased. The liquid at the contact line tended to solidify, causing the droplets to be difficult to spread and the diameter of the droplets to be smaller.

4. Conclusions

(1) Based on the MDIH, a measurement system for the gas–liquid absorption reaction and evaporation characteristics of individual slurry droplets was developed in this research. We explored the $Ca(OH)_2$ concentrations impacts, the effects of temperatures, and SO_2 concentrations on evaporation by measuring the droplet diameters, positions, and velocities. Moreover, we sampled the $Ca(OH)_2$ droplets for microscopic analysis. The holographic measurements of the proposed system allow accurate assessment of the droplets with low uncertainties.

(2) The $Ca(OH)_2$ droplets evaporation rate first increased and then decreased during the falling process, and remained constant thereafter. Compared with DI water, the evaporation rates of the $Ca(OH)_2$ droplets were lower, with average evaporation rates of about 0.676 times for the 0.08% and 0.481 times for the 0.16% (mass) $Ca(OH)_2$ droplets.

(3) The average evaporation rate of the lime slurry droplets increased significantly with an increase in temperature. In the presence of SO_2, the average evaporation rate of the lime slurry droplets was less than that without SO_2. When the SO_2 concentration was 286 mg·m^{-3}, the evaporation rate decreased with an increase in temperature.

(4) While there were large amounts of crystals in the $Ca(OH)_2$ droplets in the air, there were fewer crystals in the droplets with introducing SO_2. The crystals on the surfaces of the droplets increased significantly with introducing SO_2.

Data Availability

All data generated or analyzed during this study are included in this published article. If any researcher requests any data included in this study, it will be available upon request.

Declaration of Competing Interest

The authors declare that they have no known competing financial interests or personal relationships that could have appeared to influence the work reported in this paper.

Acknowledgements

This work was supported by the National Natural Science Fund for Distinguished Young Scholars (No. 51825605).

References

[1] C. Brogren, H.T. Karlsson, The impact of the electrical potential gradient on limestone dissolution under wet flue gas desulfurization conditions, *Chem. Eng. Sci.* 52 (18) (1997) 3101–3106.
[2] L. Wang, M.C. Zhang, Y. Huang, G.L. Xie, Y.G. Zhou, F.G. Tian,Simultaneous removal of SO2 and NO using a spray dryer absorption (SDA) method combined with O 3 oxidation for sintering/pelleting flue gas, J. Shanghai Jiaotong Univ. 39 (8) (2005) 1209–1213. (in Chinese)
[3] M.Y. Cai, X.L. Liu, T.Y. Zhu, Y. Zou, W.L. Tao, M.K. Tian, Simultaneous removal of SO_2 and NO using a spray dryer absorption (SDA) method combined with O_3 oxidation for sintering/pelleting flue gas, *J. Environ. Sci. (China)* 96 (2020) 64–71.
[4] F.F. Hill, J. Zank, Flue gas desulphurization by spray dry absorption, *Chem. Eng. Process. Process. Intensif.* 39 (1) (2000) 45–52.
[5] Q. Li, J.C. Cheng, C. Yang, Z.S. Mao, CFD-PBE-PBE simulation of an airlift loop crystallizer, *Can. J. Chem. Eng.* 96 (6) (2018) 1382–1395.
[6] M. Kadja, G. Bergeles, Modelling of slurry droplet drying, *Appl. Therm. Eng.* 23 (7) (2003) 829–844.
[7] J. Katolicky, M. Jicha, Influence of the lime slurry droplet spectrum on the efficiency of semi-dry flue gas desulfurization, *Chem. Eng. Technol.* 36 (1) (2013) 156–166.
[8] G. Krammer, H.K. Reissner, G. Staudinger, Cyclic activation of calcium hydroxide for enhanced desulfurization, *Chem. Eng. Process. Process. Intensif.* 41 (5) (2002) 463–471.
[9] H.M. Yang, S.S. Kim, Experimental study on the spray characteristics in the spray drying absorber, *Environ. Sci. Technol.* 34 (21) (2000) 4582–4586.
[10] L. Ding, B. Wu, P.C. Luo, Preparation of $CaCO_3$ nanoparticles in a surface-aerated tank stirred by a long-short blades agitator, *Powder Technol.* 333 (2018) 339–346.
[11] X.C. Wu, C. Li, J.Z. Cao, Y.X. Zhang, L.H. Chen, G. Grehan, K.F. Cen, In-situ characterization of gas–liquid precipitation reaction in a spray using rainbow refractometry, *J. Zhejiang Univ.-Sci. A* 19 (1) (2018) 86–94.
[12] C.F. Liu, S.M. Shih, R.B. Lin, Kinetics of the reaction of $Ca(OH)_2$/fly ash sorbent with SO_2 at low temperatures, *Chem. Eng. Sci.* 57 (1) (2002) 93–104.
[13] M.V. Dagaonkar, A.A.C.M. Beenackers, V.G. Pangarkar, Enhancement of gas–liquid mass transfer by small reactive particles at realistically high mass transfer coefficients: Absorption of sulfur dioxide into aqueous slurries of Ca $(OH)_2$ and $Mg(OH)_2$ particles, *Chem. Eng. J.* 81 (1–3) (2001) 203–212.
[14] H. Zhou, Y.L. Song, Q.W. Wu, Application of magnified digital in-line holography (MDIH) to the measurement of the evaporation process of desulfurization wastewater droplets in a high-temperature gas flow, *Fuel* 292 (2021) 120307.
[15] M. Sommerfeld, H.H. Qiu, Experimental studies of spray evaporation in turbulent flow, *Int. J. Heat Fluid Flow* 19 (1) (1998) 10–22.
[16] T. Li, K. Nishida, H. Hiroyasu, Droplet size distribution and evaporation characteristics of fuel spray by a swirl type atomizer, *Fuel* 90 (7) (2011) 2367–2376.
[17] D. Nguyen, D. Honnery, J. Soria, Measuring evaporation of micro-fuel droplets using magnified DIH and DPIV, *Exp. Fluids* 50 (4) (2011) 949–959.
[18] M. Seifi, C. Fournier, N. Grosjean, L. Méès, J.L. Marié, L. Denis, Accurate 3D tracking and size measurement of evaporating droplets using in-line digital holography and "inverse problems" reconstruction approach, *Opt. Express* 21 (23) (2013) 27964–27980.
[19] Middle School Chemistry National Curriculum Standard Development Group, Compulsory Education Textbook of Chemistry (Volume 2 for Grade 9), Shanghai Education Press, Shanghai (2012). (in Chinese)
[20] D. Chareyron, J.L. Marié, C. Fournier, J. Gire, N. Grosjean, L. Denis, M. Lance, L. Méès, Testing an in-line digital holography 'inverse method' for the Lagrangian tracking of evaporating droplets in homogeneous nearly isotropic turbulence, *New J. Phys.* 14 (2012) 043039.
[21] X.C. Wu, S. Meunier-Guttin-Cluzel, Y.C. Wu, S. Saengkaew, D. Lebrun, M. Brunel, L.H. Chen, S. Coetmellec, K.F. Cen, G. Grehan, Holography and micro-holography of particle fields: A numerical standard, *Opt. Commun.* 285 (13–14) (2012) 3013–3020.
[22] M. Balla, M. Kumar Tripathi, K.C. Sahu, Shape oscillations of a nonspherical water droplet, *Phys. Rev. E* 99 (2) (2019) 023107.
[23] M. Agrawal, A.R. Premlata, M.K. Tripathi, B. Karri, K.C. Sahu, Nonspherical liquid droplet falling in air, *Phys. Rev. E* 95 (3) (2017) 033111.
[24] M.K. Tripathi, K.C. Sahu, Evaporating falling drop, *Proc. IUTAM* 15 (2015) 201–206.
[25] M. Balla, M.K. Tripathi, K.C. Sahu, A numerical study of a hollow water droplet falling in air, *Theor. Comput. Fluid Dyn.* 34 (1–2) (2020) 133–144.
[26] M. Agrawal, R.K. Katiyar, B. Karri, K.C. Sahu, Experimental investigation of a nonspherical water droplet falling in air, *Phys. Fluids* 32 (11) (2020) 112105.
[27] H. Zhou, Z. Yang, Z.G. Yao, K.F. Cen, Application of digital holographic microscopy and microfluidic chips to the measurement of particle size distribution of fly ash after a wet electrostatic precipitator, *Flow Meas. Instrum.* 60 (2018) 24–29.
[28] X.C. Wu, L.C. Yao, Y.C. Wu, X.D. Lin, L.H. Chen, J. Chen, X. Gao, K.F. Cen, In-situ characterization of coal particle combustion via long working distance digital in-line holography, *Energy Fuels* 32 (8) (2018) 8277–8286.
[29] C.S. Handscomb, M. Kraft, A.E. Bayly, A new model for the drying of droplets containing suspended solids after shell formation, *Chem. Eng. Sci.* 64 (2) (2009) 228–246.
[30] J.D. Griffith, A.E. Bayly, M.L. Johns, Evolving micro-structures in drying detergent pastes quantified using NMR, *J. Colloid Interface Sci.* 315 (1) (2007) 223–229.
[31] F. Tavakoli, S.H. Davis, H.P. Kavehpour, Spreading and arrest of a molten liquid on cold substrates, *Langmuir* 30 (34) (2014) 10151–10155.
[32] R. de Ruiter, P. Colinet, P. Brunet, J.H. Snoeijer, H. Gelderblom, Contact line arrest in solidifying spreading drops, *Phys. Rev. Fluids* 2 (4) (2017) 043602.
[33] S.Y. Misyura, The crystallization behavior of the aqueous solution of $CaCl_2$ salt in a drop and a layer, *Sci. Rep.* 10 (1) (2020) 256.